Title

Pressure-tailored lithium deposition and dissolution in lithium metal batteries

Journal

Nature Energy, 6(10)

ISSN

2058-7546

Authors

Fang, Chengcheng
Lu, Bingyu
Pawar, Gorakh
et al.

Publication Date

2021-10-01

DOI

10.1038/s41560-021-00917-3

Peer reviewed

nature energy

ARTICLES

https://doi.org/10.1038/s41560-021-00917-3

Pressure-tailored lithium deposition and dissolution in lithium metal batteries

Chengcheng Fang[1,2,5]✉, Bingyu Lu[1,5], Gorakh Pawar[3], Minghao Zhang[1], Diyi Cheng[1], Shuru Chen[4], Miguel Ceja[1], Jean-Marie Doux[1], Henry Musrock[2], Mei Cai[4], Boryann Liaw[3]✉ and Ying Shirley Meng[1]✉

Unregulated lithium (Li) growth is the major cause of low Coulombic efficiency, short cycle life and safety hazards for rechargeable Li metal batteries. Strategies that aim to achieve large granular Li deposits have been extensively explored, and yet it remains a challenge to achieve the ideal Li deposits, which consist of large Li particles that are seamlessly packed on the electrode and can be reversibly deposited and stripped. Here we report a dense Li deposition (99.49% electrode density) with an ideal columnar structure that is achieved by controlling the uniaxial stack pressure during battery operation. Using multiscale characterization and simulation, we elucidate the critical role of stack pressure on Li nucleation, growth and dissolution processes and propose a Li-reservoir-testing protocol to maintain the ideal Li morphology during extended cycling. The precise manipulation of Li deposition and dissolution is a critical step to enable fast charging and a low-temperature operation for Li metal batteries.

Lithium (Li) metal is the ultimate anode material to break the specific energy bottleneck of Li-ion batteries. However, owing to its low Coulombic efficiency (CE), short cycle life and safety issues caused by dendrite growth and inactive Li formation, practical rechargeable Li metal batteries have not yet been commercialized since their inception in 1976[1–3]. It is widely accepted that the morphology is one of the determinantal factors for the CE and cycle life of Li metal batteries[4,5]. To achieve a reversible, dense Li deposition close to the actual density of Li metal (0.534 g cm^{-3}), tremendous efforts have been devoted to understand and control the Li deposition process by considering the electroplating as a mass-transport-controlled process, which is primarily affected by factors such as electrolyte properties (cation concentration, solvation structure and so on), current density and temperature[6,7]. In addition, owing to the highly reducing potential of Li, the (electro) chemically formed solid electrolyte interphase (SEI) between the Li metal and liquid electrolyte makes the electroplating a kinetically slow diffusion process. Thus, the Li deposition and dissolution are further affected by the SEI properties.

In recent decades, strategies have been extensively designed to favour at least one of the four governing factors, with the aim to improve the Li metal anode performance: first, engineering the electrolyte towards large granular Li particle deposition and a stable SEI[8–10], second, utilizing three-dimensional (3D) current collectors to increase the surface areas and reduce the local current density[11,12], third, creating an artificial SEI to facilitate Li ion transport and prevent parasitic reactions[13] and fourth, applying elevated temperature to enhance the mass transfer for enlarged Li particles growth[14]. However, the multidimensional requirements to commercialize Li metal batteries, which include a cell-level energy density of 500 Wh kg^{-1} and 1,000 cycles with 80% of capacity retention under fast charging conditions[15], can barely be achieved by solely using these approaches. Breaking the current bottleneck requires new solutions that can perfect Li deposition and dissolution on top of these achievements.

In addition to promoting the mass transport, pressurizing the electrode stack has been widely used in modern Li-ion batteries to improve cycling performance by minimizing the interfacial and transport impedance. For a Li metal anode, it was shown that increasing the uniaxial stack pressure helps to alleviate Li dendrite formation and improve the CE and cycling performance[16]. This offers a new possibility to tune the Li morphology beyond the aforementioned strategies. Moli Energy mentioned in their patent in 1985 that Li deposits formed under stack pressure showed a denser morphology with enhanced cycling efficiency[17]. Wilkinson et al.[18] examined the effect of stack pressure in Li/MoS_2 prismatic cells and attributed the Li deformation to the trade-off between the applied pressure and mechanical strength (creep strength and tensile strength) of the Li. Recent work further proved that stack pressure can effectively improve the cycling efficiency and cycle life in anode-free cells[19–21], and achieved close-packed morphology[21]. Undoubtably, applying stack pressure has been proved as an effective method to control the Li deposition morphology. The mechanical properties of Li metal have also been widely studied accordingly[22–25]. However, the underlying scientific principle of pressure effects on Li deposition and dissolution behaviour at the micro- and nanoscales, and how stack pressure can be utilized to precisely control the Li deposition and dissolution, in combination with clear experimental evidence, still need to be systematically quantified and understood. How to achieve an ideal morphology of Li deposits that comprise large Li particles seamlessly packed on the electrode, and how to achieve a very high reversibility in deposition and dissolution remain ambiguous. To answer these questions by establishing a pressure–morphology–performance correlation with

[1]Department of NanoEngineering, University of California San Diego, La Jolla, CA, USA. [2]Department of Chemical Engineering and Materials Science, Michigan State University, East Lansing, MI, USA. [3]Energy and Environmental Science and Technology Directorate, Idaho National Laboratory, Idaho Falls, ID, USA. [4]General Motors Research and Development Center, Warren, MI, USA. [5]These authors contributed equally: Chengcheng Fang, Bingyu Lu. ✉e-mail: cfang@msu.edu; boryann.liaw@inl.gov; shirleymeng@ucsd.edu

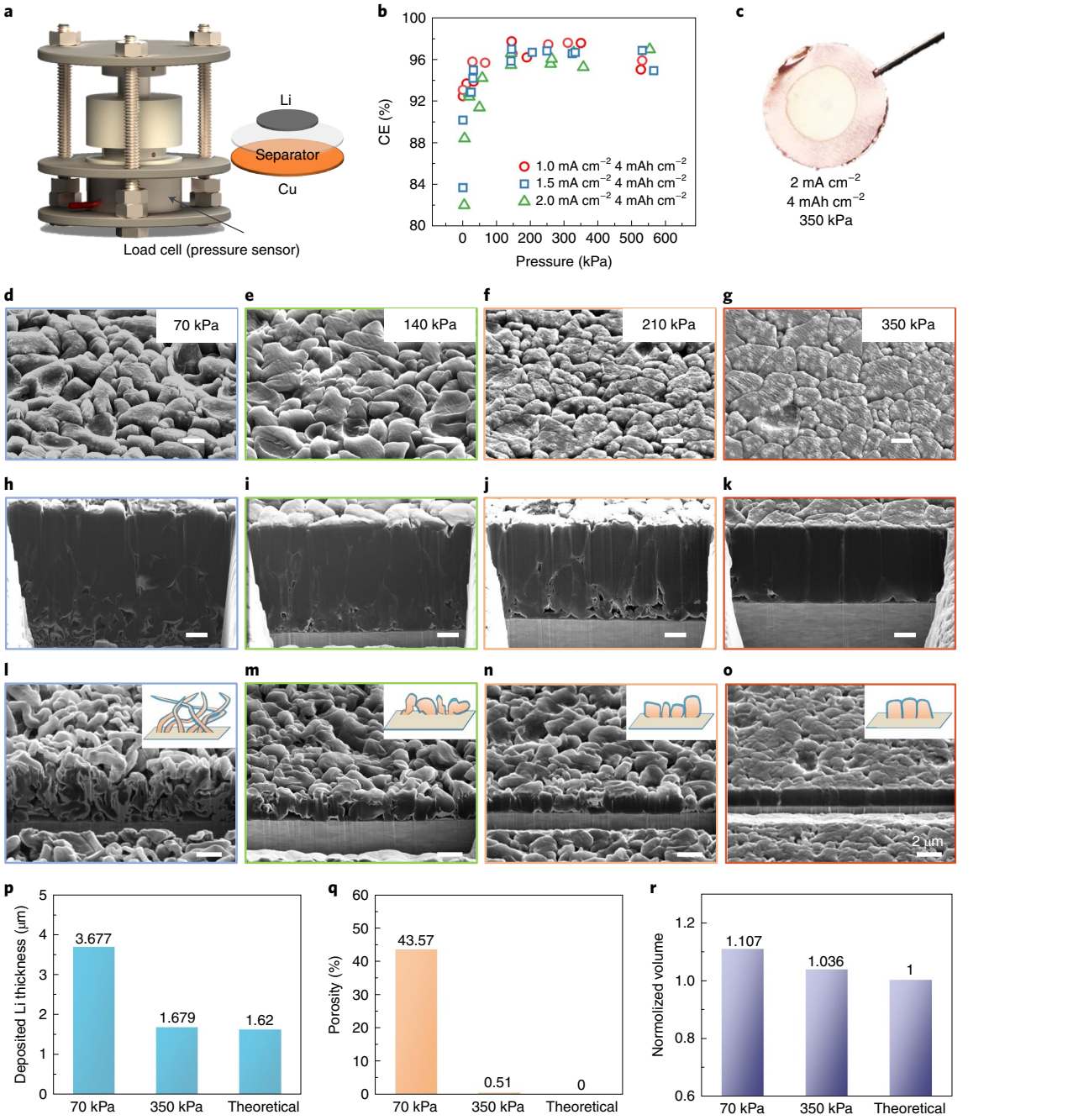

Fig. 1 | Quantifying the pressure effects on Li metal anode CE and plating morphology. a, The pressure experiment set-up, and the configuration of the Li–Cu cell. **b**, First cycle CE under different stack pressures, at current densities of 1.0, 1.5 and 2.0 mA cm^{-2}, all plated for 4 mAh cm^{-2} and stripped to 1 V. The voltage profiles for each data point are available in the source data file. **c**, Optical image of the deposited Li under a high current density (2 mA cm^{-2}), high loading (4 mAh cm^{-2}) and optimized pressure conditions (350 kPa). **d**–**k**, Top view (**d**–**g**) and cross-section (**h**–**k**) of Li deposited under 70 kPa (**d**,**h**), 140 kPa (**e**,**i**), 210 kPa (**f**,**j**) and 350 kPa (**g**,**k**) at 2 mA cm^{-2} for 1 h (2 mAh cm^{-2}). **l**–**o**, Cross-section SEM images of Li deposits at 2 mA cm^{-2} for 10 min (0.333 mAh cm^{-2}) under stack pressures of 70 kPa (**l**), 140 kPa (**m**), 210 kPa (**n**) and 350 kPa (**o**). Insets: schematic illustration of the deposited Li micromorphology. **p**–**r**, Electrode thickness (**p**), electrode porosity (**q**) and normalized volume (**r**) of pure deposited Li calculated from a 3D cryo-FIB-SEM reconstruction. Scale bars, 2 μm. Note that the actual cross-section thickness should be divided by sin 52° due to the FIB-SEM stage rotation (Methods and Supplementary Fig. 10).

the optimized Li morphology will open new opportunities to rationally design commercially viable high-energy rechargeable Li metal batteries under various environmental and operating conditions.

Here, combining 3D cryogenic focused ion beam-scanning electron microscopy (cryo-FIB-SEM), cryogenic transmission electron microscopy (cryo-TEM), titration gas chromatography (TGC)[4] and molecular dynamics (MD) simulation, we elucidated how stack pressure can be applied to precisely manipulate Li deposition and dissolution towards high performance rechargeable Li metal batteries, and so overcome the mass-transport bottleneck. Through a systematic study of the stack pressure effects on the physical morphology and chemical components of Li deposits, we identified

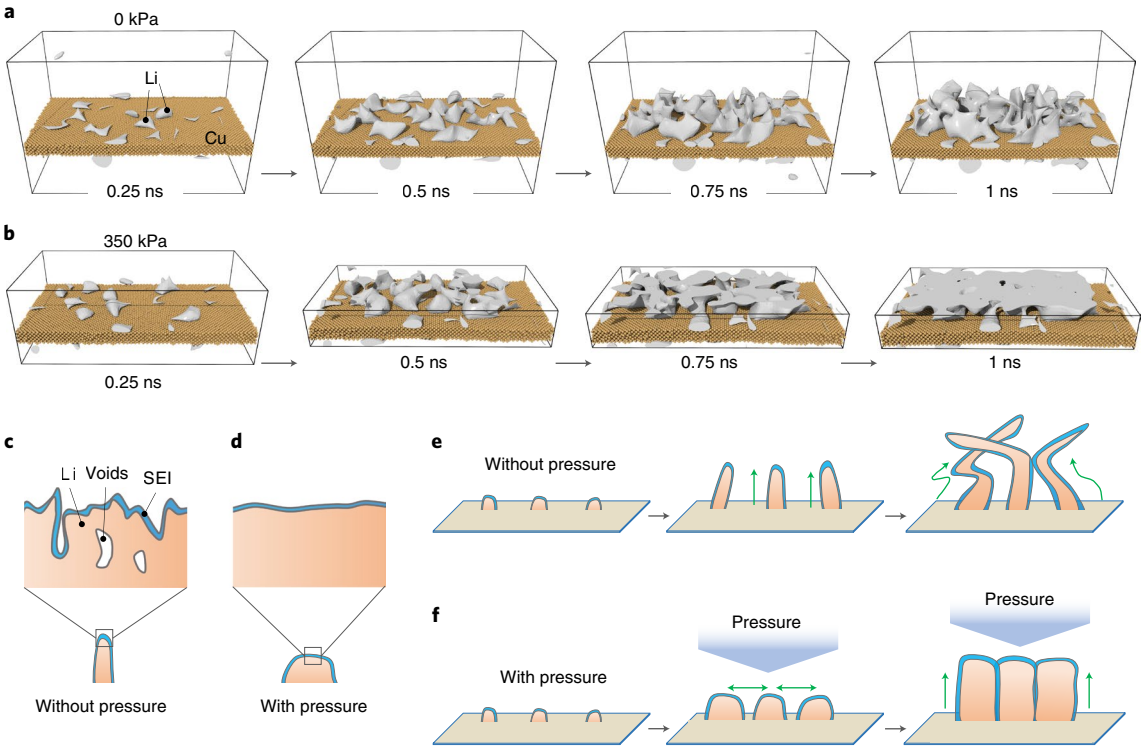

Fig. 2 | MD simulation and schematic illustration of pressure effects on Li nucleation and growth. a,**b**, The temporal evolution of Li deposition at 0 kPa (**a**) and 350 kPa (**b**) obtained with MD simulations. The cross-section of the Cu surface used for Li deposition is 25.56 × 12.77 nm^2 with a deposition rate of 20 Li ps^{-1}. Additional simulation details are given in Methods and Supplementary Discussion. **c**,**d**, Schematic illustration of the atomic-level morphology of Li under no stack pressure (**c**) and the optimal stack pressure (**d**) simulated by MD simulation. **e**, Li nucleation, initial growth and growth under no stack pressure. **f**, Li nucleation, initial growth and growth under the optimal stack pressure. The green arrows indicate the Li growth direction.

two ways in which the stack pressure regulates the Li nucleation and growth: first, tuning the favourable Li growth direction at the microscale by altering the surface energy at the Li top surface; second, densifying Li deposits at the nanoscale by exerting mechanical constraints. We found that the stack pressure induced negligible impacts on the SEI structure and components. In the stripping process, the stack pressure plays a key role to retain the electronically conductive pathway and minimize the inactive Li formation, whereas the electrochemically deposited Li reservoir is key to maintaining the dense Li structure and its reversibility on cycling. Based on a quantitative understanding, we achieved an ultradense Li deposition (99.49% electrode density) with an ideal columnar morphology and minimal surface area, and made it highly reversible on cycling with minimal inactive Li formation, and thus improved the CE (>99%) at a fast charging condition (4 mA cm^{-2}) and room temperature. Such pressure-tailored highly reversible Li metal anodes may help unlock the potential of high-energy Li metal batteries for fast charging and a wide temperature operation.

Pressure effects on Li deposition

We used a customized split cell with a load cell (Fig. 1a) to precisely control the uniaxial stack pressure applied to the battery during cycling. The pressure was set as the onset value for the electrochemical performance testing. Figure 1b shows the first cycle CE of Li–Cu cells as a function of the applied stack pressure under different current densities from 1 to 1.5 to 2 mA cm^{-2}, using an ether-based bisalt electrolyte 4.6 m lithium bis(fluorosulfonyl)imide and 2.3 m lithium bis(trifluoromethane sulfonyl)imide in 1,2-dimethoxyethane (DME)[26]. At 0 kPa, the CE decreased from 92.5% at 1 mA cm^{-2} to 82% or 89% at 2 mA cm^{-2}. When the stack pressure was slightly increased to ~35 kPa, the CE increased for all the current densities and the CE at 2 mA cm^{-2} jumped to ~92%. At 350 kPa, the CE was boosted to 98, 97 and 96% at 1, 1.5 and 2 mA cm^{-2}, respectively. Increasing the stack pressure above 350 kPa did not further improve the CE, as a higher pressure causes a severe edge effect (Supplementary Fig. 1)[27]. Please note that the optimal pressure for different electrolytes and cell set-up may slightly differ from 350 kPa. Figure 1c shows the electrochemically deposited Li at a high current density of 2 mA cm^{-2} for 4 mAh cm^{-2} exhibits a metallic silver colour.

Li–Cu pouch cells were used to test the pressure effects on long-term cycling performances. Supplementary Fig. 2a shows that a nearly doubled cycle life (116–125 cycles) was achieved for the cells tested under 350 kPa than for those (~73 cycles) under 70 kPa, when the overpotential limit was set to −0.5 V within 30 minutes as the end-of-life condition. In addition, the average CE improved from ~98 to above 99% by increasing the pressure from 70 to 350 kPa at a high current density of 4 mA cm^{-2} at room temperature (Supplementary Fig. 2b).

We then used cryo-FIB-SEM to examine the deposited Li morphology under five representative pressures: 0, 70, 140, 210 and 350 kPa. A high current density of 2 mA cm^{-2} was applied for the one-hour Li deposition (2 mAh cm^{-2}) morphological study. At 0 kPa, highly porous and whisker-like Li deposits were formed even when using the ether-based electrolyte, as shown in Supplementary Fig. 3a,b (top view and cross-section, respectively). The Li deposits become notably close-packed as the pressure increased from 70 to 350 kPa (Fig. 1d–g). The cross-section evolution was even more noticeable. As shown in Fig. 1h–k, along with the increased stack pressure, the electrode thickness obviously decreased. Especially, the cross-section morphology at 350 kPa (Fig. 1k) shows that the Li deposits formed perfect columnar structures with a large granular diameter of ~4 µm, near-theoretical thickness (9.64 µm, 2 mAh cm^{-2})

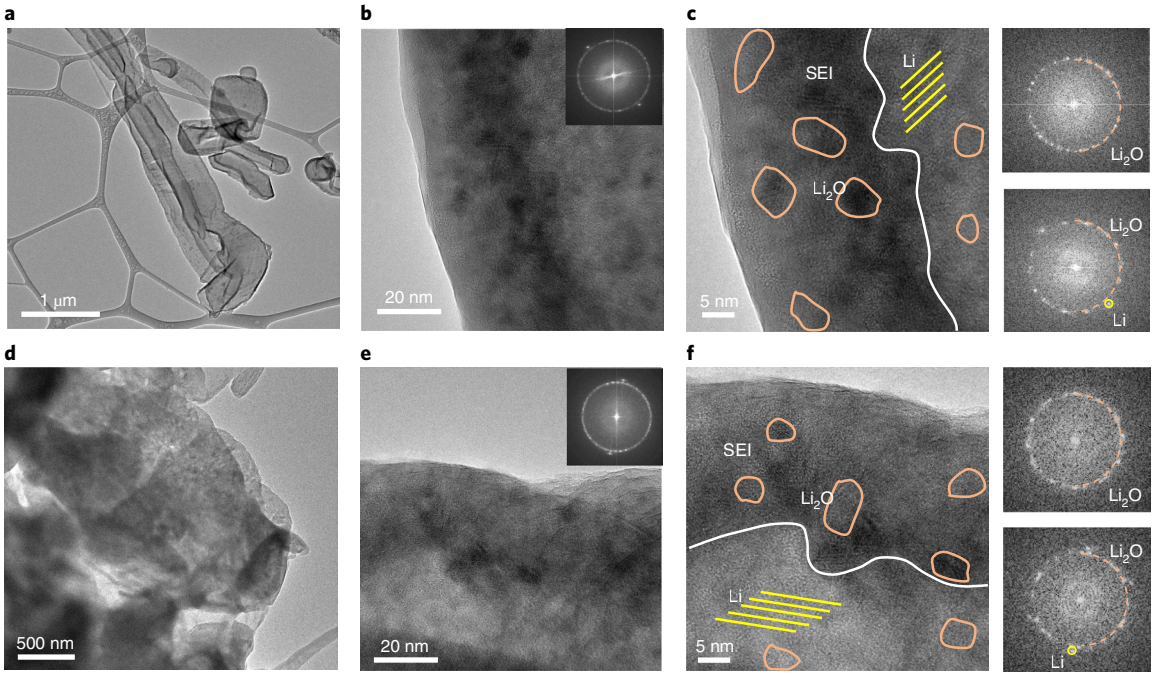

Fig. 3 | Pressure effects on SEI properties by cryo-TEM. a–c, TEM images of Li deposited at 70 kPa. **d–f**, TEM images of Li deposited at 350 kPa. Insets: fast Fourier transform patterns of the corresponding images. In **c** and **f**, the orange circles represent Li_2O nanocrystals in the SEI, the yellow lines represents crystalline Li metal and the white lines show the border between the SEI region and the deposited Li metal region. Insets: fast Fourier transform patterns that correspond to the SEI regions (top) and the deposited Li metal region (bottom). All the Li was deposited at 2 mA cm^{-2} for 5 min.

of ~10 μm (variate between 8.9 μm and 10.8 μm, Supplementary Fig. 4) and minimum electrode-level porosity, which indicates that the stack pressure can be used to precisely control the Li deposition morphology. When the deposition amount was further increased to 4 mAh cm^{-2}, which is required for a practical high-energy battery, the dense, columnar morphology was well maintained (Supplementary Fig. 5). We predicted in our previous study that the columnar Li deposits are ideal to improve the CE of Li metal by reducing the isolated metallic Li formation[4]. This study shows that columnar Li deposits can be achieved by optimizing the stack pressure.

It is worth noting that the bottom section of the Li deposits turned from relatively porous at 70 kPa (Fig. 1h) to completely dense at 350 kPa (Fig. 1k), although the top section of the Li deposits at the four different pressures were all dense, which indicates that the pressure effect plays an important role at the initial stage of Li nucleation and growth. With this assumption, we examined the pressure effects on Li nucleation and the initial growth stage with a reduced Li deposition loading at 2 mA cm^{-2} for 0.33 mAh cm^{-2} under 70, 140, 210 and 350 kPa. As shown in Fig. 1l–o, the as-formed Li nuclei showed a similar morphology as that of the bottom part of the one-hour deposits shown in Fig. 1h–k.

We further used cryo-FIB 3D reconstruction to quantify the porosity and volume of Li deposits formed under 70 and 350 kPa (Supplementary Videos 1 and 2 and Supplementary Fig. 6). Ideally, the total deposited Li (0.333 mAh cm^{-2}) should exhibit a theoretical thickness of 1.620 μm with zero porosity. When plating at 70 and 350 kPa, the Li layer thicknesses were measured to be 3.677 μm and 1.697 μm, respectively (Fig. 1p); the porosities were calculated to be 43.57 and 0.51%, respectively (Fig. 1q). Based on these numbers, the pure deposited Li volumes at 70 and 350 kPa were normalized as 1.107 and 1.036, respectively, which exceed the theoretical value of 1 (Fig. 1r). The increased volume is ascribed to the porous electrode structure, in which more Li deposits are exposed to liquid electrolyte and form SEIs with large surface areas. Eliminating the porosity of Li deposits is essential to minimize the surface exposure to liquid electrolyte, which causes extra parasitic reactions that consume the electrolyte and active Li. A similar cryo-FIB 3D reconstruction analysis was performed for Li deposits plated for 2 mAh cm^{-2} under 70 and 350 kPa (Supplementary Fig. 7).

Based on the above pressure-tailored Li deposition, we explored the possibility to overcome the mass transport limitations at a high rate and low temperature by applying stack pressure: at a higher plating rate of 4 mA cm^{-2} and room temperature, the densely packed columnar structure was still maintained under 350 kPa (Supplementary Fig. 8). At 0 °C, a very dense Li deposition could be achieved at 2 mA cm^{-2} under an increased stack pressure of 420 kPa (Supplementary Fig. 9). These results indicate that applying an optimized stack pressure is a potentially feasible way to enable the fast-charging and low-temperature operation for rechargeable Li metal batteries.

MD simulations were applied to reveal the pressure effects on the early temporal evolution of Li deposition on the Cu surface at nanoscale. The merit and appropriateness of using MD simulation to study this problem is given in the Supplementary Discussion. We compared the scenarios under 0 kPa (Fig. 2a) and 350 kPa (Fig. 2b). At 0 kPa, the Li deposition began with randomly distributed Li nucleation sites (0.25 ns in the simulation), evolved as isolated reefs (0.5 ns), grew in an uncontrolled fashion (0.75 ns), which led to a porous morphology with a poor surface coverage, uneven thickness and poor interconnectivity (1 ns, see the top-view evolution in Supplementary Fig. 11a–d). At 350 kPa, the Li nucleation (0.25 ns) and the promoted connectivity of Li nucleation sites (0.5 ns) created a Li deposition with a better homogeneity (0.75 ns) and densified layer (1 ns, see the top-view evolution in Supplementary Fig. 11e–h). Better surface area coverage by Li deposits (Supplementary Fig. 12a) and higher ordering of the Li deposit under the stack pressure is also shown by the subtle differences in the short-range Li–Li pairwise distribution function (Supplementary Fig. 12b). MD simulation reveals that stack pressure plays an important role in the temporal evolution of the Li

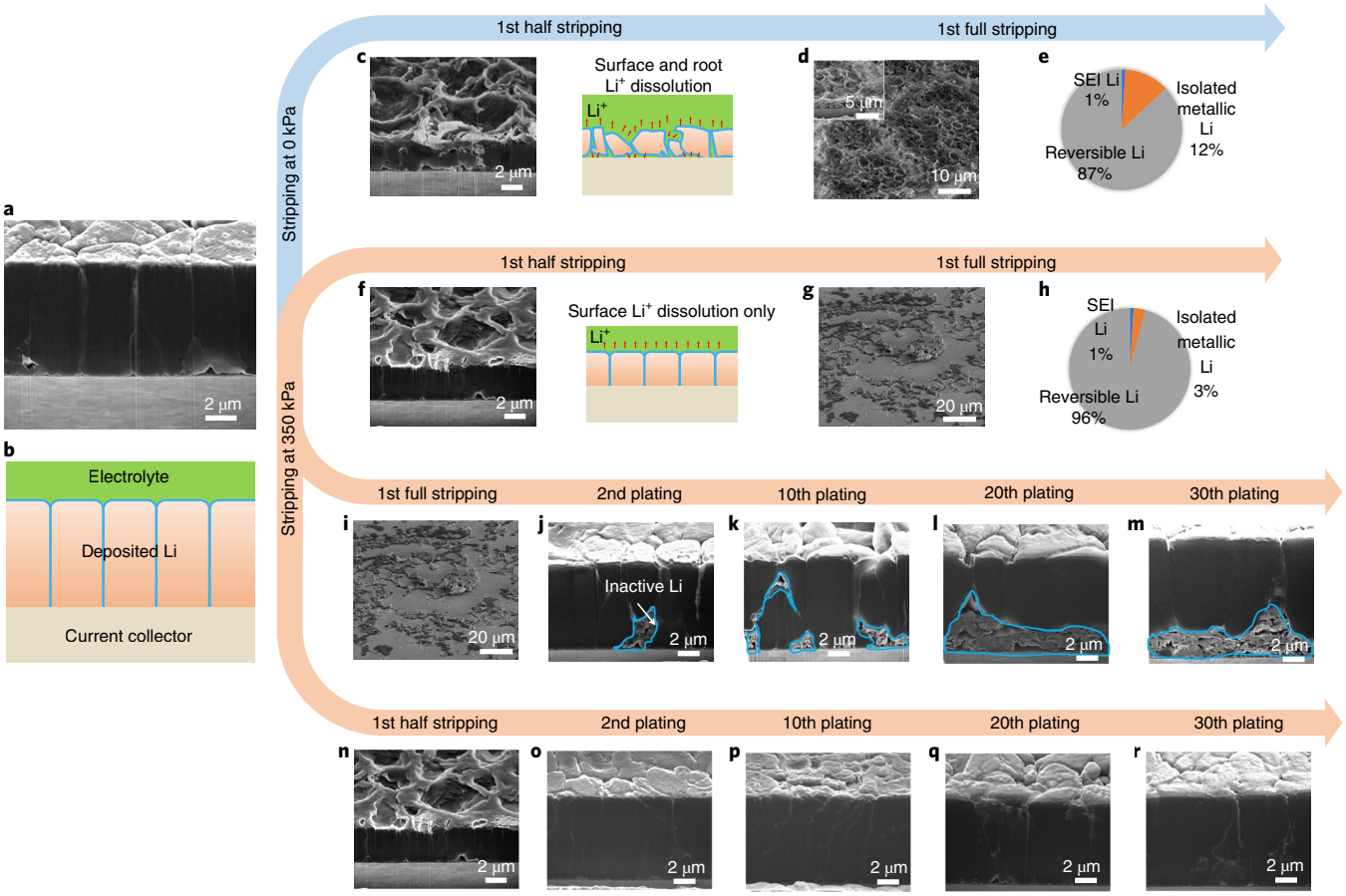

Fig. 4 | Pressure effect on Li stripping process. a,**b**, Cryo-FIB-SEM image (**a**) and schematic illustration (**b**) of columnar Li plated at 350 kPa. **c**–**e**, Li stripping at 0 kPa. **c**, Cross-section morphology (left) and schematic illustration (right) of half-stripped Li. **d**, Fully stripped Li. **e**, Capacity usage analysis by TGC. **f**–**h**, Li stripping at 350 kPa. **f**, Cross-section morphology (left) and schematic illustration (right) of half-stripped Li. **g**, Fully stripped Li. **h**, Capacity usage analysis by TGC. **i**–**r**, Li-reservoir-effect study, plating and stripping under a stack pressure of 350 kPa. **i**–**m**, Li deposition morphology evolution using the full-stripping protocol for 30 cycles. **n**–**r**, Li deposition morphology evolution using the half-stripping protocol to retain the Li reservoir for 30 cycles. All plating and stripping was at 2 mA cm^{-2} with plating for 1 h, half stripping for 30 min and full stripping to 1 V.

deposition as it promotes the lateral Li deposition and densifies the individual Li particle through smoothing the surfaces and eliminating the voids at atomic scales (Fig. 2c,d).

Such distinct Li growth behaviours and mechanisms are depicted in Fig. 2e,f. Without an effective uniaxial stack pressure, Li deposit grows freely in the vertical direction, perpendicular to the current collectors (Fig. 2e). The kinetic regime governs the deposited Li stability and morphology, due to the lower diffusion activation barrier at room temperature[28] and temporal freedom before reaching the favourable face-centred cubic hollow sites on the Cu surface. Such free-growing Li whiskers were extensively observed in previous in situ and operando studies[29,30] in which no stack pressure was present in the experimental set-up. Under a stack pressure, the nucleation and initial growth of the Li deposits adopt a lateral growth along the surface of the current collector (Fig. 2f), due to the free energy change induced by the compressive stress at the electrolyte/separator interface[31]. He et al. observed the lateral growth phenomenon using in situ TEM with an atomic force microscopy applied constraint[31]. In our case, at the critical pressure when the resistance at the interface exceeded the surface energy of growing laterally, the Li deposits turned to initially grow laterally to fill the intergranular voids, followed by growing at the interface vertically due to the limitation of space laterally and thus formed a columnar structure (Fig. 2f). In this way, Li deposits with a densely packed columnar morphology can be achieved.

Pressure effects on the SEI properties

We then used cryo-TEM to investigate the pressure effects on the SEI structure and components. We comparatively studied the Li formed under 70 and 350 kPa by plating at 2 mA cm^{-2} for five minutes in the ether-based bisalt electrolyte. The Li deposits exhibited a whisker-like morphology at 70 kPa (Fig. 3a) and a large granular morphology at 350 kPa (Fig. 3d), in accordance with the micromorphology observed by scanning electron microscopy (SEM) (Fig. 1l,o, respectively). Under both stack pressure conditions, we observed that the SEI structures and components were almost identical. Figure 3b,e compares the nanostructure of the Li deposits under 70 and 350 kPa at a large scale. Further zooming in (Fig. 3c,f) showed that the SEI thickness in both samples was 20–25 nm, with polycrystalline Li_2O embedded on the amorphous matrix with a Mosaic-type structure. More representative locations for both samples are shown in Supplementary Fig. 13. The cryo-TEM observations indicate that the stack pressure has minimum effects on the SEI structures, components and their distributions. It primarily affects the Li nucleation and growth processes.

Pressure effects on Li stripping

The pressure effects on Li stripping were systematically examined starting from the ideal columnar Li deposits formed at 2 mA cm^{-2} for one hour under 350 kPa (Fig. 4a,b). The stripping rate was 2 mA cm^{-2}. When no pressure was applied during the stripping,

a lot of voids formed in between individual Li columns, which caused liquid electrolyte to penetrate through the electrode (Fig. 4c). This facilitated the formation of inactive Li as the Li stripping occurred deep at the base of the columnar structure of the Li deposits. After fully stripping the Li to 1 V under no pressure, a substantial amount of porous inactive Li remained on the current collector (Fig. 4d). The CE was only 87%, and 12% of the deposited Li remained on the current collector in the form of isolated metallic Li measured by TGC (Fig. 4e), despite starting with fully dense Li deposits. When a stack pressure of 350 kPa was applied during the stripping, Li dissolution was constrained to the top surface only (Fig. 4f), which thus minimized the exposed surface area and reduced the inactive Li formation, as the electrolyte cannot penetrate into the roots of the dense Li deposits. After fully stripping to 1 V, only 3% of the total capacity remained as the isolated metallic Li on the current-collector surface (Fig. 4g), and the CE improved to 96% (Fig. 4h). Given that the SEI only forms during the plating process, after stripping the quantified SEI amount (1%) in these two samples remained the same (Fig. 4e,h), as they all plated at 350 kPa to form an identical dense Li. The pressure effect on the stripping process for porous Li deposits also showed the same trend, as shown in Supplementary Fig. 14. These results reveal that applying stack pressure during the stripping process helps to keep the electrode columnar structure integrity under a large ion flux. It is essential to limit the Li stripping taking place only at the top surface to prevent inactive Li formation.

Although the optimal pressure was applied, inactive Li formation was still noticeable after full stripping (Fig. 4i), due to the inevitable inhomogeneity of electrodeposited Li. When fresh Li was further deposited during the following cycle, the columnar structure was hardly maintained (Fig. 4j), ascribed to the interference from the inactive Li residue formed in previous cycles. During extended cycles, more and more inactive Li kept evolving, which broke the dense morphology (Fig. 4k–m) and consumed electrolyte and fresh Li. Importantly, we found that if the electrodeposited Li was not fully stripped in each cycle and was partially maintained as a Li reservoir (Fig. 4n), the dense, columnar morphology can be well-preserved when Li is redeposited into the reservoir during extended cycles (Fig. 4o–r). This process was enabled by following the lowest-energy Li diffusion pathway and refilling the existing SEI established during the previous cycle. The electrodeposited Li reservoir serves as the renucleation sites. In this way, minimum electrolyte and fresh Li are consumed by subsequent cycling. We further compared the replating Li morphology with 1/16th, 1/8th and 1/4 of the Li reservoir, and identified that a 1/4 reservoir is essential to maintain the dense morphology (Supplementary Fig. 15). This observation also explains well why a Li-reservoir-testing protocol always results in a higher CE[32], and a higher discharge cutoff voltage in a full cell leads to less inactive Li formation[33].

Conclusions

In summary, we identified that uniaxial stack pressure can be used as a powerful tuning knob to precisely tailor the Li deposition morphology and dissolution geometry. Using multiscale characterization tools, we discovered that applying an optimized stack pressure can fine-tune the Li nucleation and growth direction towards a dense deposition, staying away from the dendrite growth caused by mass transport limitations. We achieved the predicted ideal columnar Li deposit with minimal electrode porosity by optimizing the on-set stack pressure at 350 kPa. During the Li stripping process, pressure assured the close interfacing between the dense Li deposits and current collector to prevent the liquid electrolyte from penetrating into the root of the columnar structure, and thus dramatically reduced the inactive Li formation. The electrochemically formed dense Li reservoir is the key to maintain a columnar structure reversibly on extended cycling, which greatly improves the cycle life. Such battery electrochemical behaviours under a uniaxial stack pressure offer insights towards new design rules and new manufacturing processes for practical Li metal batteries and other metal anodes. How to integrate the stack pressure into the battery pack design without a weight penalty is a key issue to be solved towards a practical Li metal battery.

Methods

Electrochemical testing. *Li–Cu split cell test.* The split cell consists of two parts (Fig. 1a): two titanium (Ti) plungers (1/2 inch diameter or 1.27 cm) and one polyether ether ketone (PEEK) die mould (1/2 inch inner diameter). The Ti plungers were used as current collectors in the split cell because of their high electronic conductivity and high mechanical strength. The PEEK die mould was used to hold the electrochemical cell in place. All the parts were carefully machine polished so that the resistance between the Ti plunger and the inner wall of the PEEK die mould was at a minimum while providing a good seal for the electrochemical cell inside. The Cu||Li cells were assembled in an Ar-filled glove box. Cu foils (1/2-inch diameter) used in the cells were all etched by a 1 M HCl solution for 10 min followed by acetone rinsing to remove surface contaminants before being dried in the glove box antechamber under vacuum. The Cu||Li cells were made by sandwiching the Li metal foil (7 mm diameter, 50 µm thick), Celgard 2325 separator (1/2 inch diameter) and the cleaned Cu foil between the two Ti plungers inside the PEEK die mould. Only a minimum amount of electrolyte (~5 µl) was added to the Cu||Li cells to wet the separator. The bisalt electrolyte consisted of 4.6 m lithium bis(fluorosulfonyl)imide (battery grade; Oakwood Products, Inc.) + 2.3 m lithium bis(trifluoromethane sulfonyl)imide (99.95%; Sigma-Aldrich) in DME (anhydrous, >99.5%; Sigma-Aldrich). All the salts were dried under vacuum at 120 °C overnight and the solvent was dried by using molecular sieves for three days before making the electrolyte. After the assembly, the split cell and the load cell (Supplementary Fig. 16) were put into the cell holder that provided the uniaxial stacking pressure. The uniaxial stacking pressure was adjusted using the three screws on the cell holder. The screws were carefully adjusted to apply the desired stacking pressure to the split cell while keeping both the split cell and the load cell in the vertical position. The cell was tested inside the glove box using a Landt CT2001A battery cycler (Landt Instrument). Various current densities and stacking pressure were applied to conduct the study, as indicated in the main text.

Li–Cu pouch cell test. Li–Cu cells were used for the cycling performance comparison under different pressures, to make sure the Li supply in the working electrode was sufficient to exclude the influences from other parts of a battery. A Li chip of 16 mm (diameter) × 0.6 mm (thickness) (from MTI) was used as the anode and Cu foil as the cathode, with a flooded bisalt electrolyte, were used to make small Li–Cu pouch cells to perform the cycle-life evaluation under 70 and 350 kPa. The cells were discharged (Li plating) at 4 mA cm^{-2} for 30 min (2 mAh cm^{-2}), followed by charging (Li stripping) at the same current rate to 1 V. The cell was considered as reaching its 'end of life' once the discharge was automatically cutoff by a voltage limit of −0.5 V within 30 min (which resulted in Li plating at less than 2 mAh cm^{-2}) due to the increasing overpotential on cycling.

Load-cell calibration. The DYHW-116 load cell (Bengbu Dayang Sensing System Engineering Co, Ltd) was calibrated using a 100 kN Instron 5982 Universal Testing System. A known load was first applied to the load cell to calibrate it at the high end of its range. Then, the accuracy of the calibration was verified by comparing, at different loads over the total range of the load cell, the values reported by the experimental set-up with the load applied by the testing system.

Cryogenic focused ion beam scanning electron microscopy. The Cu foil with deposited Li was obtained from the split cell and then washed with DME to remove the residual electrolyte in the Ar-filled glove box. The sample was mounted on a SEM stub (Ted Pella) in the glove box, then transferred to a FEI Scios DualBeam FIB/SEM system with an airtight transfer holder to minimize air exposure. Liquid nitrogen was used to cool down the sample stage to −180 °C to create a cryogenic environment that minimized beam damage to the sample. A gallium ion beam with a voltage of 30 kV, current of 7 nA and dwell time of 100 ns was used to roughly mill down the cross-section of the deposited Li. After the rough milling, the cross-section was cleaned with an ion beam at 1 nA. The SEM image of the cross-section was taken using an Everhart–Thornley detector at 5 kV and 0.1 nA.

Three-dimensional reconstruction of the cryo-FIB-SEM images. A series of cross-sectional SEM images was taken to reconstruct the 3D bulk structure of the deposited Li. First, a rough cross-sectional milling (30 kV, 7 nA) was done on the deposited Li. After that, the left and right sides of the cross-section were milled away to single out the region of interest (14 µm × 4 µm × 4 µm). Two cross marks were then made by milling near the region of interest, one on the top left corner and the other on the left-side cross-sectional wall, to serve as correctional landmarks for the automatic slicing and imaging. The region of interest and the landmarks were selected in the Auto Slices & View G3 software (Thermo Fisher

Scientific), which controlled the automatic slicing and imaging. Slices (40 at 100 nm thick each) of the cross-section were acquired at 30 kV and 0.5 nA and the SEM image of each slice was taken with an Everhart–Thornley detector at 5 kV and 0.1 nA. The 40 slices of cross-sectional images were then integrated in the Amira-Avizo software (Thermo Fisher Scientific) to reconstruct the 3D bulk structure of the deposited lithium. The voids and Li volumes were also calculated using the Amira-Avizo software based on contrast difference. The electrode density was calculated based on the ratio of the Li metal volume and the electrode volume (sum of the voids volume and the Li metal volume).

Cryogenic transmission electron microscopy. The cryo-TEM samples were prepared by peeling the Li deposited under different pressures from Cu foils onto the TEM grids. Samples from 75 and 350 kPa cells were tested at a current density of 2 mA cm^{-2} to plate Li for 5 min. In the Ar-filled glove box, the TEM samples were slightly rinsed with DME to remove trace Li salts. Once dried, the samples were sealed in airtight bags and plunged directly into a bath of liquid nitrogen. The airtight bags were then cut and the TEM grids were immersed in liquid nitrogen immediately. Then, the grids were mounted onto a TEM cryoholder (Gatan) via a cryotransfer station. In short, the whole TEM sample preparation and transfer process prevented any contact of Li metal with the air at room temperature. TEM characterizations were carried out on JEM-2100F at 200 kV. High-resolution TEM images were taken at a magnification of ×500K with a Gatan OneView Camera (full 4K×4K resolution) when the temperature of the samples reached about 100 K. Fast Fourier transform patterns were analysed using DigitalMicrograph software.

Titration gas chromatography. The TGC method[4] was used to quantify the amount of inactive metallic Li formed after cycling under different conditions. After the Li was plated and stripped under the desired condition, the Cu||Li cell was recovered from the split cell and the Cu foil with residual inactive Li together with the separator were put into a 30 ml bottle without washing. The bottle was then sealed with a rubber stopper and metal wires to prevent the generated gas from leaking and minimize the safety hazards. The internal pressure of the bottle was then adjusted to 1 atm by connecting the bottle and the glove-box environment, whose internal pressure was adjusted to 1 atm, with an open-ended syringe needle. After taking out the bottle from the glove box, an excessive amount (0.5 ml) of deionized water was injected into the bottle and the residual inactive metallic Li reacted with the deionized water to form hydrogen (H_2) gas. The as-generated gas was then well-mixed by shaking and a gas-tight syringe was used to quickly take 30 µl of the gas from the sealed bottle. The gas was then injected into a Nexis GC-2030 Gas Chromatograph (Shimadzu) for the H_2 measurement. A pre-established H_2 calibration curve was used to calculate the mass of inactive metallic Li from the measured H_2 peak area. With the conversion between mAh and mg of Li shown in the following equations, the percentage of inactive metallic Li formed after stripping in the total amount of the Li plated was calculated:

$$1\,\mathrm{C} = 1\,\mathrm{A} \times \mathrm{s} = 1,000\,\mathrm{mA} \times 1/3,600\,\mathrm{h} = 1/3.6\,\mathrm{mAh} \quad (1)$$

$$1\,\mathrm{C} = 6.25 \times 10^{18}\ \text{electrons} = 1.038 \times 10^{-5}\ \text{mol electrons} \quad (2)$$

$$\mathrm{Li}^{+} + \mathrm{e}^{-} = \mathrm{Li} \quad (3)$$

$$1\,\mathrm{mAh} = 3.7368 \times 10^{-5}\,\mathrm{mol\,Li} = 0.2594\,\mathrm{mg\,Li} \quad (4)$$

Molecular dynamics simulation of Li deposition. MD simulations were used to decipher the temporal evolution of Li deposition on a Cu surface under applied uniaxial stacking pressures of 0 and 350 kPa. Newton's equations of motion were solved to obtain the temporal positions of the Cu and Li atoms. The Cu substrate used in the simulations comprised 25,200 Cu atoms arranged in a face-centred cubic lattice structure with a domain of 12.77 nm (length)×25.56 nm (width)×1.3 nm (height).

An initial energy minimization of the Cu surface was performed with 0 and 10^{-8} eV Å^{-1} energy and force cutoff, respectively. The Li deposition was directed to the Cu surface at a deposition rate of 20 Li ps^{-1}. The Li deposition was simulated in an isothermal–isobaric ensemble at 300 K with a time step of 1 fs and a cutoff distance of 10 Å under a stipulated uniaxial stack pressure (0 or 350 kPa). The Li–Li and Cu–Cu atomic interactions were simulated with the modified embedded atom method interatomic potentials[34,35], whereas the Li–Cu interactions were modelled with the Lennard–Jones 6–12 interatomic potentials with the following Lennard–Jones potential parameters: $\varepsilon_{\mathrm{Cu-Li}} = 0.047$ eV and $\sigma_{\mathrm{Cu-Li}} = 2.182$ Å. These Li–Cu parameters were obtained by the Lorentz–Berthelot arithmetic mixing rules:

$$\varepsilon_{\mathrm{Cu-Li}} = \sqrt{\varepsilon_{\mathrm{Cu-Cu}}\varepsilon_{\mathrm{Li-Li}}} \quad (5)$$

$$\sigma_{\mathrm{Cu-Li}} = \frac{(\sigma_{\mathrm{Cu-Cu}} + \sigma_{\mathrm{Li-Li}})}{2} \quad (6)$$

from the available Lennard–Jones potential parameters for the pure Li (ref. [34]) and Cu (ref. [35]) atoms. The LAMMPS (large-scale atomic/molecular massively parallel simulator) MD simulation package[36] was used to perform all the simulations, whereas the atomic scale trajectory information was visualized by using the Open Visualization Tool (Ovito)[37].

The Cu surface area occupied by Li was calculated by summation of the partial area covered by the deposited Li within a stipulated distance (here, 1.5× van der Waal's radius of the Li atom (1.82 Å) was used) on the Cu surface. The Li–Li pairwise distribution function was generated with a cutoff distance and bin size of 10 Å and 0.1 Å, respectively. The magnitude of the Li–Li pairwise distribution function at 0 kPa was shifted downwards by a factor of 4.8 compared with that at 350 kPa. Such a difference should account for the empty space in the simulation box when the Li–Li pairwise distribution function was generated. The surface Li solid mesh was constructed with a virtual probe sphere of radius 3 Å and the virtual probe sphere was used to quantify the amount of Li volume that could be filled within the Li deposit.

Finally, we explain the implications of the MD simulations based on the computational Li deposition rate in comparison with the experimental Li deposition rate at 2 mA cm^{-2} to give a proper perspective and context of their relevance. To compare the two very different rates in the temporal progression, we used the mass/charge conservation as the basis to explain the relevance. In the MD simulations, a total of 19,031 Li atoms was deposited on the Cu surfaces with a total deposition area of 652.8 nm^2 over 1 ns at 350 kPa. This deposition rate was equivalent to 2.92×10^{15} Li cm^{-2} ns^{-1} in the MD simulation. However, the total number of Li atoms deposited during the experimental study at 2 mA cm^{-2} over 10 min is equivalent to 1.25×10^{16} Li cm^{-2} s^{-1}. Therefore, based on the mass/charge conversation principle, the experimental Li deposition rate at 2 mA cm^{-2} for 10 min is equivalent to a computational deposition rate of 20 Li ps^{-1} for 4.28 ns in the MD simulation. Thus, the overall morphological evolutions between the experimental observations and MD simulations should be relatively relevant.

Data availability

All the data generated in this study are included in the published article and its supplementary information. Source data are provided with this paper.

Received: 6 June 2021; Accepted: 8 September 2021;
Published online: 18 October 2021

References

1. Cheng, X. B., Zhang, R., Zhao, C. Z. & Zhang, Q. Toward safe lithium metal anode in rechargeable batteries: a review. *Chem. Rev.* **117**, 10403–10473 (2017).
2. Fang, C., Wang, X. & Meng, Y. S. Key issues hindering a practical lithium–metal anode. *Trends Chem.* **1**, 152–158 (2019).
3. Winter, M., Barnett, B. & Xu, K. Before Li ion batteries. *Chem. Rev.* **118**, 11433–11456 (2018).
4. Fang, C. et al. Quantifying inactive lithium in lithium metal batteries. *Nature* **572**, 511–515 (2019).
5. Xu, W. et al. Lithium metal anodes for rechargeable batteries. *Energy Environ. Sci.* **7**, 513–537 (2014).
6. Chazalviel, J. N. Electrochemical aspects of the generation of ramified metallic electrodeposits. *Phys. Rev. A* **42**, 7355–7367 (1990).
7. Xiao, J. How lithium dendrites form in liquid batteries. *Science* **366**, 426–427 (2019).
8. Cao, X. et al. Monolithic solid–electrolyte interphases formed in fluorinated orthoformate-based electrolytes minimize Li depletion and pulverization. *Nat. Energy* **4**, 796–805 (2019).
9. Yang, Y. et al. High-efficiency lithium-metal anode enabled by liquefied gas electrolytes. *Joule* **3**, 1986–2000 (2019).
10. Chen, S. et al. High-voltage lithium-metal batteries enabled by localized high-concentration electrolytes. *Adv. Mater.* **1706102**, 1706102 (2018).
11. Niu, C. et al. Self-smoothing anode for achieving high-energy lithium metal batteries under realistic conditions. *Nat. Nanotechnol.* **14**, 594–601 (2019).
12. Cao, D. et al. 3D Printed high-performance lithium metal microbatteries enabled by nanocellulose. *Adv. Mater.* **31**, 68–71 (2019).
13. Xu, R. et al. Artificial interphases for highly stable lithium metal anode. *Matter* **1**, 317–344 (2019).
14. Wang, J. et al. Improving cyclability of Li metal batteries at elevated temperatures and its origin revealed by cryo-electron microscopy. *Nat. Energy* **4**, 664–670 (2019).
15. Liu, J. et al. Pathways for practical high-energy long-cycling lithium metal batteries. *Nat. Energy* **4**, 180–186 (2019).
16. Hirai, T. Influence of electrolyte on lithium cycling efficiency with pressurized electrode stack. *J. Electrochem. Soc.* **141**, 611 (1994).
17. Brandt, K. & Stiles, J. A. R. Battery and methods of making the battery. US Patent 5114804-A (1985).
18. Wilkinson, D. P., Blom, H., Brandt, K. & Wainwright, D. Effects of physical constraints on Li cyclability. *J. Power Sources* **36**, 517–527 (1991).
19. Yin, X. et al. Insights into morphological evolution and cycling behaviour of lithium metal anode under mechanical pressure. *Nano Energy* **50**, 659–664 (2018).

20. Louli, A. J. et al. Exploring the impact of mechanical pressure on the performance of anode-free lithium metal cells. *J. Electrochem. Soc.* **166**, 1291–1299 (2019).
21. Weber, R. et al. Long cycle life and dendrite-free lithium morphology in anode-free lithium pouch cells enabled by a dual-salt liquid electrolyte. *Nat. Energy* **4**, 683–689 (2019).
22. Zhang, X. et al. Rethinking how external pressure can suppress dendrites in lithium metal batteries. *J. Electrochem. Soc.* **166**, 3639–3652 (2019).
23. Masias, A., Felten, N., Garcia-Mendez, R., Wolfenstine, J. & Sakamoto, J. Elastic, plastic, and creep mechanical properties of lithium metal. *J. Mater. Sci.* **54**, 2585–2600 (2019).
24. Xu, C., Ahmad, Z., Aryanfar, A., Viswanathan, V. & Greer, J. R. Enhanced strength and temperature dependence of mechanical properties of Li at small scales and its implications for Li metal anodes. *Proc. Natl Acad. Sci. USA* **114**, 57–61 (2017).
25. Wang, Y., Dang, D., Xiao, X. & Cheng, Y. T. Structure and mechanical properties of electroplated mossy lithium: effects of current density and electrolyte. *Energy Storage Mater.* **26**, 276–282 (2020).
26. Alvarado, J. et al. Bisalt ether electrolytes: a pathway towards lithium metal batteries with Ni-rich cathodes. *Energy Environ. Sci.* **12**, 780–794 (2019).
27. Lee, H. et al. Electrode edge effects and the failure mechanism of lithium-metal batteries. *ChemSusChem* **11**, 3821–3828 (2018).
28. Gaissmaier, D., Fantauzzi, D. & Jacob, T. First principles studies of self-diffusion processes on metallic lithium surfaces. *J. Chem. Phys.* **150**, 41723 (2019).
29. Ghassemi, H., Au, M., Chen, N., Heiden, P. A. & Yassar, R. S. Real-time observation of lithium fibers growth inside a nanoscale lithium-ion battery. *Appl. Phys. Lett.* **99**, 123113 (2011).
30. Zeng, Z. et al. Visualization of electrode–electrolyte interfaces in $LiPF_6$/EC/DEC electrolyte for lithium ion batteries via in situ TEM. *Nano Lett.* **14**, 1745–1750 (2014).
31. He, Y. et al. Origin of lithium whisker formation and growth under stress. *Nat. Nanotechnol.* **14**, 1042–1047 (2019).
32. Adams, B. D., Zheng, J., Ren, X., Xu, W. & Zhang, J. G. Accurate determination of Coulombic efficiency for lithium metal anodes and lithium metal batteries. *Adv. Energy Mater.* **8**, 1702097 (2017).
33. Louli, A. J. et al. Diagnosing and correcting anode-free cell failure via electrolyte and morphological analysis. *Nat. Energy* **5**, 693–702 (2020).
34. Ponce, V., Galvez-Aranda, D. E. & Seminario, J. M. Analysis of a Li-ion nanobattery with graphite anode using molecular dynamics simulations. *J. Phys. Chem. C* **121**, 12959–12971 (2017).
35. Xu, Z. & Buehler, M. J. Nanoengineering heat transfer performance at carbon nanotube interfaces. *ACS Nano* **3**, 2767–2775 (2009).
36. Plimpton, S. Fast parallel algorithms for short-range molecular dynamics. *J. Comput. Phys.* **117**, 1–19 (1995).
37. Stukowski, A. Visualization and analysis of atomistic simulation data with OVITO—the Open Visualization Tool. *Model. Simul. Mater. Sci. Eng.* **18**, 015012 (2010).

Acknowledgements

This work was supported by the Office of Vehicle Technologies of the US Department of Energy through the Advanced Battery Materials Research (BMR) Program (Battery500 Consortium) under contract DE-EE0007764. Cryo-FIB was performed at the San Diego Nanotechnology Infrastructure (SDNI), a member of the National Nanotechnology Coordinated Infrastructure, which is supported by the National Science Foundation (grant ECCS-1542148). We acknowledge the UC Irvine Materials Research Institute (IMRI) for the use of the cryo-TEM, funded in part by the National Science Foundation Major Research Instrumentation Program under grant CHE-1338173. Idaho National Laboratory is operated by Battelle Energy Alliance under contract no. DE-AC07-05ID14517 for the US Department of Energy. The US Government retains and the publisher, by accepting the article for publication, acknowledges that the US Government retains a non-exclusive, paid-up, irrevocable, worldwide license to publish or reproduce the published form of this manuscript, or allow others to do so, for US Government purposes. We thank J. K. Greene for the lithium surface coverage area data analysis, and Y. Lin for the simulation results discussion.

Author contributions

C.F. and Y.S.M. conceived the ideas. C.F. designed the experiments. B. Lu implemented the electrochemical tests. B. Lu, C.F. and D.C. performed the cryo-FIB experiments. G.P. and B. Liaw performed the MD simulations. M.Z. collected the cryo-TEM data. C.F. conducted TEM data interpretation. S.C. and M. Cai conducted the pouch cell tests. M. Ceja prepared the electrolytes. J.-M.D. conducted the load-cell design and calibration. C.F. wrote the manuscript. All the authors discussed the results and commented on the manuscript. All the authors gave approval to the final version of the manuscript.

Competing interests

The authors declare no competing interests.

Additional information

Supplementary information The online version contains supplementary material available at https://doi.org/10.1038/s41560-021-00917-3.

Correspondence and requests for materials should be addressed to Chengcheng Fang, Boryann Liaw or Ying Shirley Meng.

Peer review information *Nature Energy* thanks Venkatasubramanian Viswanathan for their contribution to the peer review of this work.